BOREAS An international journal of Quaternary research

A post-IR IRSL chronology and dust mass accumulation rates of the Nosak loess-palaeosol sequence in northeastern Serbia

ZORAN M. PERIĆ, SLOBODAN B. MARKOVIĆ, GYÖRGY SIPOS, MILIVOJ B. GAVRILOV, CHRISTINE THIEL, CHRISTIAN ZEEDEN AND ANDREW S. MURRAY

BOREAS

Perić, Z. M., Marković, S. B., Sipos, G., Gavrilov, M. B., Thiel, C., Zeeden, C. & Murray, A. S. 2020 (October): A post-IR IRSL chronology and dust mass accumulation rates of the Nosak loess-palaeosol sequence in northeastern Serbia. *Boreas*, Vol. 49, pp. 841–857. https://doi.org/10.1111/bor.12459. ISSN 0300-9483.

In the Middle Danube Basin, Quaternary deposits are widely distributed in the Vojvodina region where they cover about 95% of the area. Major research during the last two decades has been focused on loess deposits in the Vojvodina region. During this period, loess in the Vojvodina region has become one of the most important Pleistocene European continental climatic and environmental records. Here we present the dating results of 15 samples taken from the Nosak loess-palaeosol sequence in northeastern Serbia in order to establish a chronology over the last three glacial–interglacial cycles. We use the $pIRIR_{290}$ signal of the 4–11 μm polymineral grains. The calculated ages are within the error limits partially consistent with the proposed multi-millennial chronostratigraphy for Serbian loess. The average mass accumulation rate for the last three glacial–interglacial cycles is 265 $g\ m^{-2}\ a^{-1}$, which is in agreement with the values of most sites in the Carpathian Basin. Our results indicate a highly variable deposition rate of loess, especially during the MIS 3 and MIS 6 stages, which is contrary to most studies conducted in Serbia where linear sedimentation rates were assumed.

Zoran M. Perić (zoranperic.geo@gmail.com), Research Group for Terrestrial Paleoclimates, Max Planck Institute for Chemistry, Hahn-Meitner Weg 1, Mainz 55128, Germany; Slobodan B. Marković, Serbian Academy of Sciences and Arts, Knez Mihajlova 35, Belgrade 11000, Serbia and Chair of Physical Geography, Faculty of Sciences, University of Novi Sad, Trg Dositeja Obradovića 3, Novi Sad 21000 Serbia; György Sipos, Department of Physical Geography and Geoinformatics, University of Szeged, Szeged, Hungary; Milivoj B. Gavrilov, Chair of Physical Geography, Faculty of Sciences, University of Novi Sad, Trg Dositeja Obradovića 3, Novi Sad 21000 Serbia; Christine Thiel, Centre for Nuclear Technologies, Technical University of Denmark, Risø Campus, Frederiksborgvej 399, Roskilde DK-4000, Denmark and Federal Institute for Geosciences and Natural Resources, Stilleweg 2, Hannover 30655, Germany; Christian Zeeden, Leibniz Institute for Applied Geophysics, Stilleweg 2, Hannover 30655, Germany; Andrew S. Murray, Nordic Laboratory for Luminescence Dating, Department of Geoscience, Aarhus University, Risø Campus, Frederiksborgvej 399, Roskilde DK-4000, Denmark; *received 3rd November 2019, accepted 24th May 2020.*

The focus of most Quaternary research conducted in Serbia to date was related to the loess plateaus situated in the Vojvodina region. These studies contributed to the better understanding of climate changes during the Pleistocene in this part of Europe (e.g. Marković *et al.* 2008, 2015; Obreht *et al.* 2019). However, beside these extensive and continuous loess-palaeosol sequences, there are also numerous loess areas in the southeastern, central and northeastern parts of the country (Marković *et al.* 2014a; Obreht *et al.* 2014, 2016). These sequences appear as smaller, isolated loess spots and do not show the continuity that is recorded in the loess plateaus in the Vojvodina region, which was one of the reasons why these sites remained almost unexplored. Nevertheless, recent findings revealed that, beside unique fossil records (Dimitrijević *et al.* 2015; Tomić *et al.* 2015), these loess sequences contain an exceptional record of palaeoclimatic and palaeoenvironmental conditions during the Quaternary, on the transitional zone between the Balkan region and the Carpathian Basin.

One of the most important sites in this region is the Nosak loess-palaeosol section located in the Kostolac Coal Basin. The Kostolac Basin hosts the second largest active lignite mine in Europe, where extensive coal exploitation began at the end of the 19th century, and continues until this day (Dimitrijević *et al.* 2015). The coal mining has led to several archaeological, palaeontological and geological findings, raising the public interest in this region. The most significant discoveries to date have been a Kostolac steppe mammoth skeleton from Middle Pleistocene fluvial deposits, discovered in 2009 (Lister *et al.* 2012) and the later finding of a rich palaeontological layer, including further steppe mammoth fossils from the latest Middle Pleistocene loess-palaeosol succession, in 2012 (Marković *et al.* 2014a; Dimitrijević *et al.* 2015; Tomić *et al.* 2015). The discovery of the mammoth skeletons, after which the mining operations in this area came to a temporary halt, gave us the opportunity to further investigate the Nosak loess-palaeosol profile. At the site, environmental magnetic analyses, malacological analysis, general reconstruction of environmental dynamics, preliminary luminescence dating of two samples and ESR dating of an enamel plate removed from a mandibula mammoth tooth were performed (e.g. Marković *et al.* 2014a; Dimitrijević *et al.* 2015). These studies yielded valuable results, which established the Nosak section as one of the most significant representative records of Middle and Late Pleistocene palaeoclimate and palaeoenvironment dynamics as well

DOI 10.1111/bor.12459

as mammoth distribution in this region (Marković *et al.* 2014a).

The most critical requirements for retrieving accurate climate records are independent chronologies and sedimentation rates. In order to establish the first chronology of the Nosak loess-palaeosol sequence, we are employing a two-step post-IR IRSL (Thomsen *et al.* 2008) protocol. This method has been proven to produce a stable elevated temperature IRSL signal recorded after a preceding lower temperature IR stimulation, and seemingly does not suffer from anomalous fading, which is commonly an undesirable effect in feldspar IRSL (Huntley & Lamothe 2001). One further advantage of this approach is the ability to date material from the last three glacial–interglacials, as opposed to quartz OSL dating, which cannot be used to reliably date samples from Serbian loess records beyond a D_e value of ~120 Gy (36 ka; Perić *et al.* 2019).

This study aims to establish the first luminescence-based chronology of a site in northeastern Serbia from the last three glacial–interglacial cycles and investigate the past dust activity in this area by calculating the MARs for the Nosak loess-palaeosol sequence.

Regional setting

The Nosak loess-palaeosol sequence is situated in northeastern Serbia (latitude 44°44″31′N, longitude 21°15″28′E) in a lowland region at the southeastern limit of the great Carpathian (Pannonian, Middle Danube) Basin in between the Danube and Mlava rivers (17 km north from the city of Požarevac) (Fig. 1). This area is also referred to as the Kostolac Basin, which is enclosed by the Danube River to the north, the Velika Morava River to the west, while to the east the Basin extends to the Požarevačka greda, a geological structure that rises over an alluvial plain of the Danube and Mlava rivers (Dimitrijević *et al.* 2015).

The Basin was formed during the Lower through Upper Miocene due to strong tectonic movements (faulting) during the formation of the Pannonian Basin alongside favourable peat-forming conditions (Marković *et al.* 2014a; Muttoni *et al.* 2018). The base of the Kostolac Basin is composed of Devonian crystalline rocks and is covered by Neogene sediments. The total thickness of the Neogene sediments ranges from 300 to 5000 m in the central part of the depression (Marković *et al.* 2014a).

Litho- and pedostratigraphy

At the Nosak section, modern soil (S0) and four recent glacial loess units L1, L2, L3 and L4 associated with several weakly developed interstadial soils, as well as interglacial pedocomplexes S1, S2 and S3 are present (Fig. 2). The nomenclature for this chronostratigraphy follows the Danubian loess stratigraphical model developed by Marković *et al.* (2015). This model was established to correlate the loess-palaeosol units of the Danube Basin with the Chinese Loess plateau stratigraphy 'L and S' labelling system (e.g. Kukla 1987; Kukla & An 1989). The modern soil (S0) covering the top of the section is represented by a 90-cm-thick chernozem layer (10 YR 4/2 – colour is determined for dry samples using the Munsell soil colour chart). The 870-cm-thick Last Glacial loess unit L1 (10 YR 7/3) is intercalated with numerous weakly developed palaeosols (10 YR 5/3). The last interglacial pedocomplex S1 is 295 cm thick and composed of a lower dark Ah horizon indicating a fossil chernozem formation (10 YR 4/2) overlain by a middle lighter A horizon (10 YR 5/3) and the uppermost weakly developed A horizon (10 YR 5/2) characterized by numerous crotovinas. The underlying succession has a thickness of ~600 cm and contains the penultimate glacial L2 loess unit (10 YR 7/3), intercalated with numerous weakly developed palaeosols (Marković *et al.* 2014a). This loess unit covers a double pedocomplex (S2) including a lower strongly developed S2SS2 fossil cambisol B horizon that is gradually transformed to an upper altered A horizon (7.5 YR 5/8) and upper weakly developed A horizon (S2SS1; 7.5 YR 5/8) intercalated by a darker loessic layer (S2LL1). The approximately 150-cm-thick L3 loess, which is in a zone close to the boundary with palaeosol S2SS2, is heavily bioturbated and rich in carbonate concretions. The lowermost pedocomplex S3 is ~180 cm thick and has a very similar morphology to the upper S2SS2 fossil cambisol. The lowermost, 50-cm-thick L4 loess has many carbonate concretions and humic infiltrations in fossil root channels. At the transitional zone between the palaeosol S2SS1 and the overlying L2 loess, a palaeontological layer was discovered (Marković *et al.* 2014a).

Sampling, preparation and facilities

The sampling was performed during the palaeontological excavations in 2012, after the discovery of the palaeontological layer and the mammoth skeleton by the research team from the Institute of Archaeology at the Serbian Academy of Sciences and Arts. The samples for luminescence dating were recovered by hammering black PVC tubes (15 cm long and 5 cm in diameter) into the face of the freshly cleaned profile (Fig. 3). In total, 15 samples were collected where most of the samples yielded enough polymineral grains for D_e measurements. The samples were processed in the Nordic Laboratory for Luminescence Dating (NLL), Aarhus University, Risø Campus, Denmark, under subdued orange light. The inner material of the cylinders was used for equivalent dose measurements (conducted at the Luminescence Dating Laboratory, University of Szeged, Hungary) and the outer, light-exposed material for the water content and dose rate determination (conducted at the NLL).

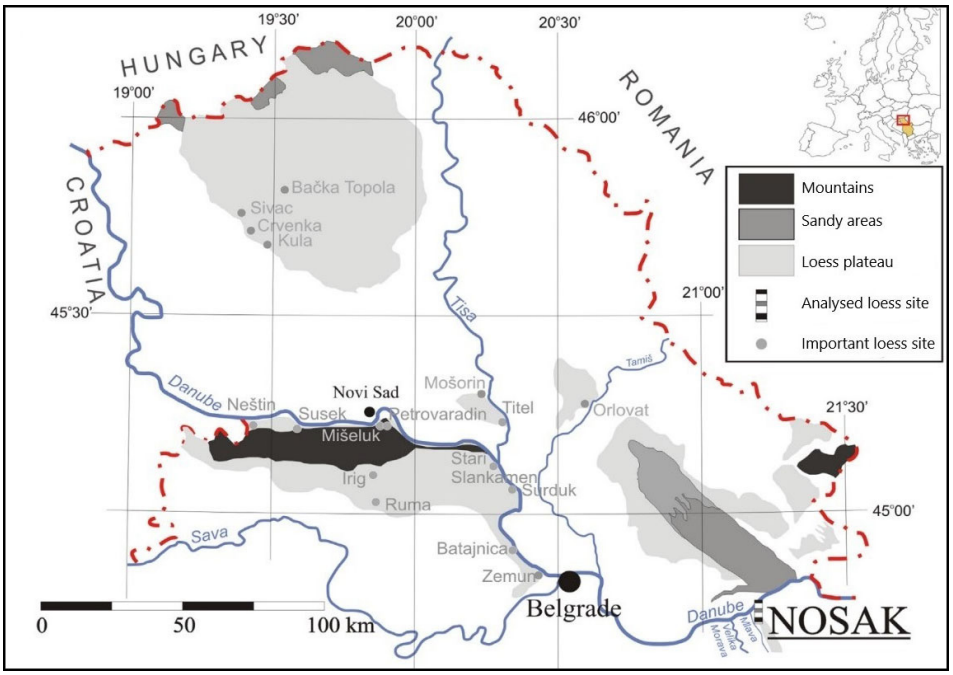

Fig. 1. Map of the loess distribution in the Vojvodina and adjacent regions showing the geographical position of the Nosak section and other main loess sites (modified from Marković *et al.* 2012). [Colour figure can be viewed at www.boreas.dk]

The inner, non-light-exposed material was sieved through 90, 63 and 40 μm sieves. The <40 μm material was first treated with 32% HCl to remove carbonates followed by a 30% H_2O_2 treatment to remove organic matter, and finally with sodium oxalate ($Na_2C_2O_4$) to avoid aggregation. The 4–11 μm polymineral fine grains were extracted by settling according to Stoke's law. The fine-grained quartz was obtained by immersing a part of the polymineral samples in 32% fluorosilicic acid (H_2SiF_6) for 7 days. Finally, in order to remove fluorides, the grains were rinsed with 32% HCl. Unfortunately, we were not able to extract a sufficient amount of quartz grains to produce any reliable data. After every treatment step, the samples were washed 3–5 times with deionized water. Subsequently, the polymineral grains were settled on 9.8 mm stainless steel cups with acetone (~2 mg L^{-1}) using the pipette method. Luminescence measurements for the polymineral extracts were conducted on an automated Risø TL/OSL DA20 reader, equipped with a $^{90}Sr/^{90}Y$ beta source calibrated for quartz fine grains (Bøtter-Jensen *et al.* 2010). The stimulation of the polymineral grains employed IR (870 nm; ~140 mW cm^{-2}) LEDs with the IRSL signal detected through a Schott BG-39/CN-7-59 glass filter combination. The equivalent doses of all the samples were measured using a single aliquot regenerative (SAR) $pIRIR_{290}$ protocol (Table 1). The choice of the first IR stimulation temperature was part of the pre-investigations and is discussed below. All the luminescence data were analysed using the Risø Analyst software, version 4.31.9.

Dose rate measurements

For the dose rate determination, the sediment was first dried at 50 °C, then crushed (<200 μm) using a ring-grinder, ignited at 450 °C for 24 h to remove organic matter, and finally cast in wax in Marinelli-type moulds to retain ^{222}Rn. The solid cup moulded samples were then stored for >3 weeks to allow ^{222}Rn to build up to equilibrium with ^{226}Ra. Subsequently, the concentrations of ^{238}U, ^{232}Th and ^{40}K were determined by analysing the samples for >24 h on a gamma spectrometer with a high-purity Germanium detector at the NLL. The calibration of the spectrometers is presented in Murray *et al.* (1987). The radionuclide concentrations were converted to dry dose rates according to the conversion factors presented by Guérin *et al.* (2011). The activities of ^{238}U, ^{226}Ra, ^{232}Th and ^{40}K are shown in Table 2 and Fig. 4. The contribution of cosmic rays to the total dose rate was calculated according to Prescott & Hutton (1994), using depth, altitude, density, latitude and longitude for each sample, assuming an uncertainty of 5%. The field water content was measured directly on the samples. However, in several cases, the calculated water content displayed very low values. For the middle part of the profile (L1-S1), the water content varied between 1% (samples 133056 and 133057) and 7% (sample 133053). Such low values may be the result of the exposure of the Nosak section to air for a long period of time prior to sampling. For this reason, we do not consider the measured water content

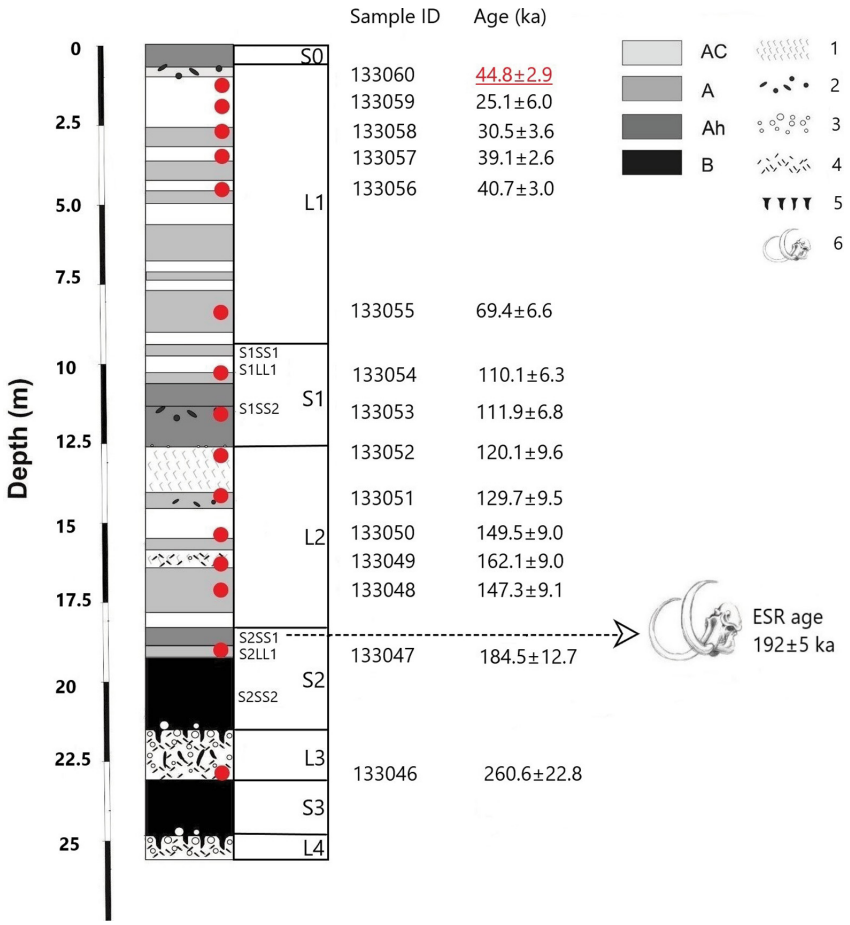

Fig. 2. Revised lithology of Nosak section, position of the luminescence samples (red circles) together with the pIRIR ages and the ESR age (for details see text). The rejected pIRIR age is highlighted in red. AC = transitional horizon between initial pedogenesis and background sediment; A = initial pedogenetic horizon; Ah = accumulated humus horizon; B = cambisol; 1 = carbonate pseudomycelia; 2 = crotovinas; 3 = carbonate concretions; 4 = hydromorphic features; 5 = former root channels filled with humic material; 6 = palaeontological layer. Modified from Marković *et al.* (2014a, b). [Colour figure can be viewed at www.boreas.dk]

to be reliable estimates over the geological time. Thus, based on field observations and previous studies conducted in this region (Schmidt *et al.* 2010; Antoine *et al.* 2009), the water content was estimated to be 12±5% and was assumed to apply throughout the burial period. For the 4–11 μm polymineral grains an internal α dose rate contribution from U and Th of 0.08±0.02 was assumed (Rees-Jones 1995).

Disequilibrium between ^{238}U and ^{226}Ra was not detected in any sample (average of the ^{238}U to ^{226}Ra ratio is 1.03±0.24), except for the lowermost sample (133046 – 2320 cm depth). Here, a disequilibrium was observed with a calculated ratio of 7.33±24.81. The reason for this may be associated with the groundwater, as indicated by hydromorphic features and bioturbation at the depth where the sample was collected. The dose rates for the polymineral fraction range from 2.58± 0.10 Gy ka^{-1} for sample 133046, to 4.37± 0.19 Gy ka^{-1} for sample 133048. The resulting total dose rates do not vary significantly with depth (except for sample 133046), and are summarized in Fig. 4 and Table 2.

Post-IR IRSL measurements

In order to establish the temperature for a stable pIRIR signal, we tested the dependence of D_e on the first stimulation temperature on 15 aliquots of the sample 133057. The results of the IR stimulation plateau showed that there are no significant variations of the pIRIR$_{290}$ D_e with temperature. The pIRIR$_{290}$ signal intensity did not display a considerable decrease with increasing first IR stimulation temperature and we can conclude that even for first IR stimulation temperatures as low as 50 °C and as high as 250 °C, the intensity of the signals is sufficient to allow precise measurements of the D_e (Fig. 5). However, the most stable signal was observed at the first IR stimulation temperature of 200 °C. Based on these observations, the pIRIR$_{200,\ 290}$ signal was chosen for all polymineral measurements in this study.

Fig. 3. The Nosak loess-palaeosol sequence with the position of the palaeontological layer. Revised from Marković *et al.* (2014a, b). [Colour figure can be viewed at www.boreas.dk]

After a preheat of 320 °C for 60 s, the aliquots were stimulated twice with IR diodes for 200 s. During the first stimulation, the temperature was kept at 200 °C (IR signal), while the second IR stimulation temperature was held at 290 °C (post-IR IRSL signal, $pIRIR_{200,\ 290}$). The test dose signal (~40 to ~260 Gy) was measured in the same way. At the end of each measurement cycle, a high-temperature IR clean-out at 325 °C for 200 s was carried out. All aliquots were measured 'one at a time'. For each sample, at least six aliquots were measured, except for samples 133052 and 133051 (five aliquots per sample), as we were not able to extract a greater amount of 4–11 μm polymineral grains. For the calculation, the signal from the initial 2 s of stimulation, less a background from the last 50 s, was used. The dose response curves were fitted with single exponential functions using Analyst version 4.31.9. A representative dose response and decay curve for the $pIRIR_{200,\ 290}$ signal are presented in Fig. 6.

Table 1. Single aliquot regenerative (SAR) protocol used for D_e measurements.

Step	A $pIRIR_{200,\ 290}$	B IR_{50}
1	Give dose	Give dose
2	Preheat 320 °C for 60 s	Preheat 250 °C for 60 s
3	IRSL 200 °C for 200 s	IRSL 50 °C for 200 s → L_x
4	IRSL 290 °C for 200 s → L_x	–
5	Give test dose	Give test dose
6	Preheat 320 °C for 60 s	Preheat 250 °C for 60 s
7	IRSL 200 °C for 200 s	IRSL 50 °C for 200 s → T_x
8	IRSL 290 °C for 200 s → T_x	–
9	IR bleach at 325 °C for 200 s	IRSL 290 °C for 200 s
10	Return to step 1	Return to step 1

In every measurement, we included the standard recycling and recuperation tests (Wintle & Murray 2006). Recycling ratios within a maximum deviation of 10% from unity were considered acceptable, as was a recuperation signal amounting to less than 5% of the natural signal. The aliquots that did not meet these criteria were rejected and not used in the age calculation. The average D_0 value for all the accepted aliquots was ~567 Gy. The uncertainty on D_e was calculated as the standard error of the mean. The average SAR $pIRIR_{290}$ recycling ratio (99 aliquots from 15 samples) is 1.03±0.02. Recuperation and recycling ratios are presented in Table 2.

To test the ability of the $pIRIR_{200,\ 290}$ to accurately measure laboratory doses given prior to any laboratory heat treatment, a dose recovery test was performed on bleached aliquots (24 h in a Hönle SOL2 solar simulator) of sample 133057. Doses ranging from 100 to 800 Gy were administered (three aliquots per dose), and then measured in the same manner as the equivalent dose. The test dose was set between 30 and 50% of the given dose. Three aliquots were measured to determine the residual dose for this sample after bleaching in the solar simulator. The residual dose was 25±1 Gy and was subtracted from the measured D_e. The result of this test is presented in Fig. 7 and shows that our SAR $pIRIR_{200,\ 290}$ protocol is able to successfully recover laboratory doses up to at least ~800 Gy. From the results of the dose recovery test, it was noticeable that the best measured to given dose ratio (6% of unity) was found when the test dose of ~30% of the total dose was applied. The ratio was higher (~9–10% of unity) when the test dose of ~50% of the total dose was employed. Similar results are presented in the study of Yi *et al.* (2016), where it was concluded that the ideal

Table 2. Summary of depth information, sample codes, dry alpha, beta and gamma dose rates, radionuclide concentrations, total dose rates, weighted mean D_e values, recycling ratios, recuperation, luminescence ages and total errors in ka for the Nosak section. *n* represents the number of aliquots. The systematic errors taken into account include: 2% beta source calibration, 3% conversion factors, 3% gamma spectrometer calibration, 5% water content and 15% cosmic radiation. Error terms are given as 1 standard error.

Depth (cm)	Sample code	Alpha $\dot{D}$ (Gy ka^{-1})	Beta $\dot{D}$ (Gy ka^{-1})	Gamma $\dot{D}$ (Gy ka^{-1})	^{238}U (Bq kg^{-1})	^{226}Ra (Bq kg^{-1})	^{232}Th (Bq kg^{-1})	^{40}K (Bq kg^{-1})	Total $\dot{D}$ (Gy ka^{-1})	D_e (Gy)	Recycling ratio	Recuperation (% cor. nat)	*n*	Age (ka)	Total error (ka)
105	133060	0.11±0.00	1.51±0.04	0.72±0.02	37.8±11.9	45.8±1.1	54.3±1.0	439±15	3.91±0.16	178.6±8.5	1.045±0.015	2.56±0.27	10	44.8±2.9	3.03
185	133059	0.25±0.01	2.23±0.05	1.51±0.04	53.3±7.5	50.9±0.8	57.3±0.9	522±11	4.25±0.18	109.9±25.0	1.040±0.016	−1.91±1.12	6	25.1±6.0	6.00
285	133058	0.24±0.01	2.22±0.05	1.510±.04	42.6±11.8	37.8±1.1	42.2±0.9	413±15	3.49±0.14	109.7±11.8	1.033±0.021	2.51±0.62	6	30.5±3.6	3.66
345	133057	0.22±0.01	2.12±0.07	1.38±0.04	41.6±7.0	43.6±0.7	49.0±0.8	436±10	3.74±0.15	149.5±7.8	1.053±0.022	1.59±1.04	6	39.1±2.6	2.76
440	133056	0.21±0.01	1.98±0.04	1.34±0.04	31.5±8.5	43.9±0.8	48.8±0.9	440±11	3.74±0.15	155.6±9.2	1.035±0.022	3.82±0.55	6	40.7±3.0	3.12
855	133055	0.21±0.01	1.86±0.04	1.23±0.03	45.2±12.3	42.3±1.1	53.1±1.0	457±16	3.79±0.16	266.5±22.4	1.033±0.018	1.43±0.83	10	69.4±6.6	6.77
1005	133054	0.22±0.01	1.89±0.04	1.29±0.04	42.8±12.6	47.5±1.2	49.5±1.1	480±17	3.86±0.17	428.7±16.2	1.041±0.016	0.83±1.25	8	110.1±6.3	6.73
1160	133053	0.22±0.01	1.94±0.07	1.31±0.04	46.4±13.1	41.9±1.2	52.0±1.1	513±18	3.91±0.17	440.5±18.5	0.998±0.022	1.85±0.89	6	111.9±6.8	7.15
1315	133052	0.22±0.01	1.86±0.07	1.29±0.04	44.2±7.1	41.5±0.7	51.9±0.8	498±11	3.85±0.16	465.4±31.2	1.058±0.024	−0.37±0.69	5	120.1±9.6	9.88
1440	133051	0.22±0.01	1.81±0.06	1.28±0.04	58.3±7.4	40.2±0.7	48.8±0.6	472±11	3.70±0.15	483.6±29.0	1.040±0.021	0.80±1.51	5	129.7±9.5	9.91
1560	133050	0.21±0.01	1.70±0.05	1.23±0.04	32.7±7.1	40.3±0.7	53.3±0.8	552±11	4.00±0.17	600.8±25.7	1.040±0.020	1.71±0.38	6	149.5±9.0	9.53
1650	133049	0.21±0.01	1.73±0.04	1.23±0.04	49.0±13.0	39.2±1.1	54.6±1.3	585±18	4.09±0.18	666.7±22.8	0.993±0.009	2.11±0.15	6	162.1±9.0	9.57
1725	133048	0.19±0.01	1.61±0.06	1.09±0.03	32.0±7.7	44.2±0.7	59.9±0.9	630±13	4.37±0.19	647.7±28.3	1.022±0.016	2.39±0.24	6	147.3±9.1	9.59
1920	133047	0.25±0.01	2.07±0.05	1.44±0.04	47.5±7.5	45.7±0.7	61.8±0.9	598±12	4.33±0.19	802.7±43.0	0.983±0.027	1.34±0.41	6	184.5±12.7	13.29
2320	133046	0.23±0.01	1.77±0.06	1.30±0.04	2.7±9.3	20.1±0.8	29.3±0.8	297±13	2.58±0.10	674.6±53.9	1.003±0.023	2.17±0.52	7	260.6±22.8	23.91

test dose size when applying pIRIR at 290 °C is 30% of the measured dose. Based on our observations and Yi *et al.* (2016), the test dose size for all our D_e measurements was kept at ~30% of the measured dose.

Despite the good dose recovery test results, the calculated residual dose appeared to be surprisingly high. Various authors have reported that the bleaching of high temperature pIRIR signals is more problematic than the bleaching of low temperature IRSL signals (Li & Li 2011; Buylaert *et al.* 2012). It was suggested that a longer exposure of the samples to sunlight or a solar simulator can reduce the pIRIR signals significantly. However, in several studies, it has been shown that the residual dose measured after bleaching in a solar simulator is not consistent with the residual dose after bleaching in sunlight (e.g. Stevens *et al.* 2011). Bleaching of aeolian dust in nature is likely to be conducted over repeated intervals and to take place over much longer times than in the laboratory, meaning that the $pIRIR_{290}$ signal can be reset to a negligible value (Buylaert *et al.* 2012; Yi *et al.* 2015). To test this and possibly determine a lower residual dose for the D_e calculations than the one established for the dose recovery test, we exposed six aliquots of the sample 133046 to direct sunlight over a period of 30 days. The aliquots were kept in a glass Petri dish and placed outside during the months of June and July. The calculated residual dose in this case was 3.4±0.4 Gy, confirming that natural sunlight is able to reset the $pIRIR_{290}$ signal far more efficiently than the solar simulator. This remaining D_e value, which is negligible compared to the measured D_es, was assumed to be an unbleachable residual dose and was subsequently subtracted from all D_e results prior to the age calculation.

In several studies (e.g. Buylaert *et al.* 2012, 2015; Roberts 2012) where the $pIRIR_{290}$ signals from both sand-sized K-rich feldspar and polymineral fine grains have been investigated, evidence has been presented that fading uncorrected $pIRIR_{290}$ ages show a very good agreement with independent age control for a world-wide set of samples. In the study of Buylaert *et al.* (2012), fading tests on three quartz samples and the standard Risø calibration quartz were performed. The test yielded a mean $g_{2\ days}$ value of 0.98±0.08% per decade. Such a fading rate would result in age underestimates of ~10% when employing a standard fading model. These findings suggest that the $pIRIR_{290}$ signal is unlikely to suffer from fading to a greater degree than the quartz OSL fast component. Even though in some studies (e.g. Lauer *et al.* 2017) a detectable fading value was observed when using the $pIRIR_{290}$ signal, most fading rates were <2, and the mean value (16 samples: 3–6 aliquots per sample) of all obtained *g*-values was 1.6±0.1. According to Buylaert et al. (2012) even in such cases where there exists a detectable fading when employing the pIRIR290 signal, this may be an artefact related to the measurement procedure. Consequently, the ages are less reliant on the

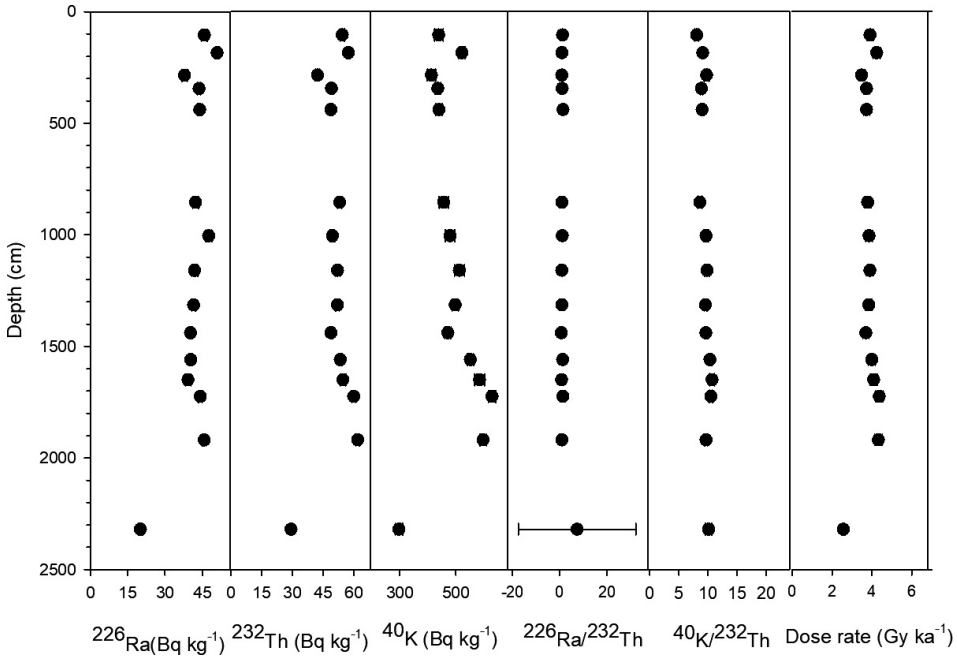

Fig. 4. Summary of the radionuclide activity concentrations measured using high resolution gamma spectrometry and the derived total dose rates. The analytical data are presented in Table 2.

assumptions included in the fading correction models. In our study, such a fading correction would not improve the calculated ages, which is why we do not attempt any fading correction.

Incomplete bleaching detection

The calculated ages in most cases show a stratigraphically consistent increase, ranging from 261±23 ka (sample 133046) to 25±6 ka (sample 133059), except for the uppermost sample (taken at the S0–L1 boundary), which displayed an age overestimation of ~30 ka, possibly because of incomplete bleaching. The most reliable way to test if a younger sample is affected by poor bleaching is to compare the pIRIR ages with the ages obtained from blue OSL on quartz grains. However, no usable amount of quartz fine grains could be recovered from the Nosak samples, which is why we were not able to perform this comparison. An alternative method to examine whether the $pIRIR_{290}$ signal is likely to have been fully reset is comparison with other IR signals that have different sensitivities to daylight. It is known that the IR_{50} signal bleaches more rapidly in sunlight than IR signals stimulated at elevated temperatures (Thomsen *et al.* 2008) or the $pIRIR_{290}$ signal (Buylaert *et al.* 2012; Murray *et al.* 2012). In order to test whether sample 133060 was actually not fully reset, we exposed 42 aliquots of the polymineral fine grains to artificial sunlight in a solar simulator for different lengths of time, ranging from 1 to 100 000 s. Subsequently, we measured the relative bleaching of the IR_{50} and $pIRIR_{290}$ signals using protocols presented in Table 1. The results of the test (Fig. 8) showed that the IR_{50} signal bleaches at a significantly faster rate than the $pIRIR_{290}$ signal. After 10 000 seconds of bleaching, the normalized IR_{50} signal was reduced to ~7% of the natural, while the equivalent $pIRIR_{290}$ signal displayed a decrease of barely ~40%. The $pIRIR_{290}$ to IR_{50} ratio of the natural measured D_e in this case was 1.4 ($pIRIR_{290}$ – 151 Gy; IR_{50} – 107 Gy), which lies outside the 10% rejection criterion and is consistent

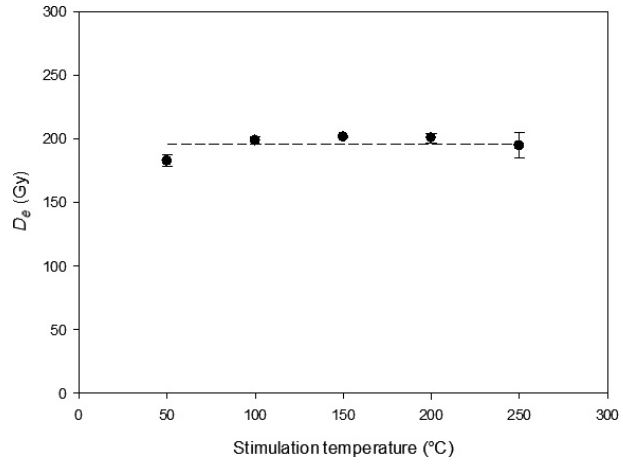

Fig. 5. First IR stimulation plateau for sample 133057 (345 cm depth). The results display no significant trend of D_e with increasing first IR stimulation temperature, which suggests that the unstable IR signal can be removed at first IR stimulation temperatures as low as 50 °C (Buylaert *et al.* 2012). The error bars represent one standard error.

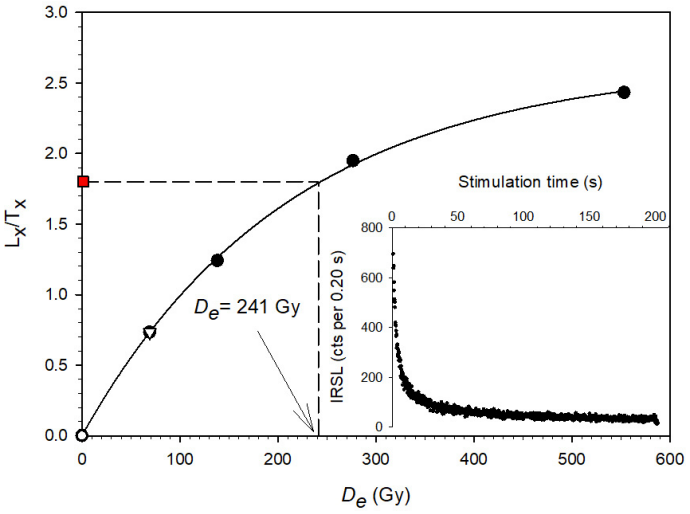

Fig. 6. Representative sensitivity corrected $pIRIR_{290}$ dose response curve for an aliquot of sample 133055 (855 cm depth). The dose response curve was fitted with a single saturating exponential function. The D_e value for this aliquot was provided by interpolating the sensitivity corrected natural luminescence level on the dose response curve (dashed line). The open triangle represents the remeasured dose point (to provide the recycling ratio), the open circle is the response to a zero dose (recuperation) and the red square shows the sensitivity corrected IRSL of the natural signal. The inset shows the natural $pIRIR_{290}$ decay curve for the same aliquot. [Colour figure can be viewed at www.boreas.dk]

with the assumption that the $pIRIR_{290}$ is less well bleached than the corresponding IR_{50} signal. In the studies of Thiel *et al.* (2011) and Buylaert *et al.* (2013), similar IR_{50} to $pIRIR_{290}$ D_e ratios for some of their samples were reported, where it was suggested that the reason for this may be incomplete bleaching of the $pIRIR_{290}$ signal during postdepositional reworking.

Given that the sample was recovered at the S0–L1 boundary, we have to also consider the possibility that the $pIRIR_{290}$ protocol is not suited for dating Holocene samples and that using post-IR IRSL stimulation at lower temperatures would yield a more consistent age. In the study of Kars *et al.* (2014) measurements of young samples using the $pIRIR_{290}$ showed large variations in residual doses. In some cases, the residual dose even exceeded the equivalent dose. In the same study, based on the presented data, it has been advised that for dating young sediments, a low temperature pIR protocol should be used and for the identification of well-bleached coarse grains the single grain dating method (Reimann *et al.* 2012; van Gorp *et al.* 2013). Unfortunately, in this case, we are not able to perform any additional measurements because of the lack of material. In order to get more clarity on the problems stated above, high sampling resolution dating must be applied, preferably using quartz OSL dating.

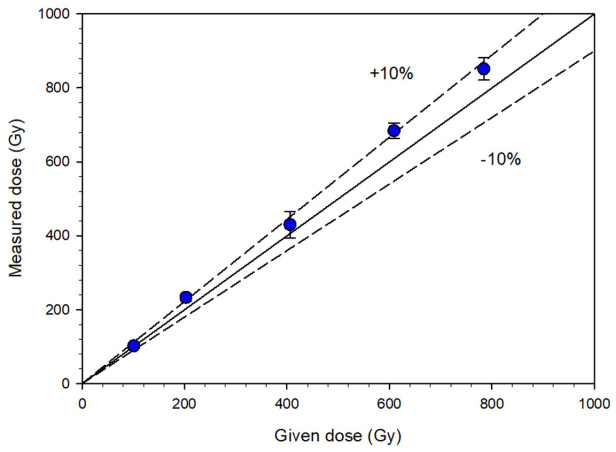

Fig. 7. Results of the dose recovery test on sample 133057. The solid line indicates the ideal 1:1 dose recovery ratio while the dashed lines bracket a 10% variation from unity. Doses ranging from ~100 to 800 Gy were administered with test doses set at 30–50% of the given dose. Three aliquots were measured per dose point. The average given to measured dose ratio was 1.08±003. Error bars represent one standard error. [Colour figure can be viewed at www.boreas.dk]

Nevertheless, here we argue that the sample 133060 is most likely incompletely bleached due to postdepositional processes and choose to reject and not consider it for further analysis. At this point, we have to state that we cannot exclude the possibility that some of the other samples could also be affected by incomplete bleaching. However, we do not find it likely, given that the all of the calculated ages passed the conducted internal tests and in most cases show a fairly good agreement with the expected ages and are stratigraphically consistent.

Age-depth modelling

The luminescence ages allow the development of a continuous and fully independent age vs. depth model for the Nosak site. At this point, we have to underline that the sampling resolution is not high enough to detect slight accumulation variations and hiatuses; however, it is

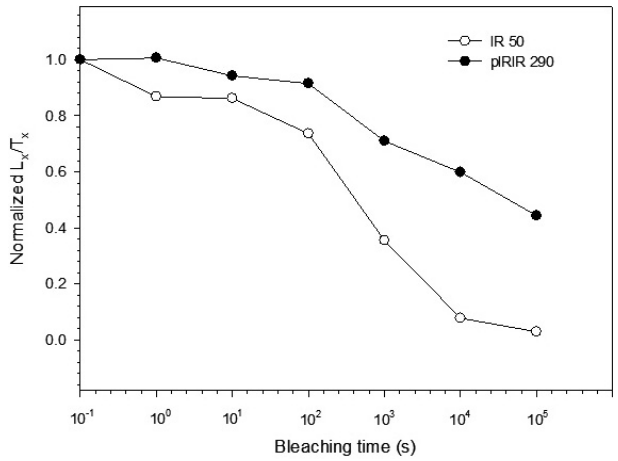

Fig. 8. Post-IR IR_{290} and IR_{50} bleaching curves measured for sample 133060 using protocols A and B in Table 1, respectively. Aliquots were exposed for different lengths of time to artificial light in a solar simulator after which we measured their sensitivity-corrected luminescence. The data are normalized to the natural sensitivity corrected luminescence (zero exposure time). Each data point is the average of three aliquots.

sufficient to identify general accumulation trends and patterns of dust deposition.

The methods for developing continuous age-depth models from discrete luminescence age points differ in the literature (e.g. Újvári *et al.* 2014; Kang *et al.* 2015; Stevens *et al.* 2016; Zeeden *et al.* 2018) and most of them are based on contrasting assumptions. Here we chose to implement the ADmin age-depth model (Zeeden *et al.* 2018) based on 14 $pIRIR_{200,\ 290}$ data points, which was designed specifically for application to luminescence dates. Contrary to other methods (e.g. Bacon model of Blaauw & Christen 2011) the ADmin age-depth model does not make any assumptions on sedimentation rates. We first created a density function for random and systematic uncertainty from the data set, assuming that both ages and uncertainties are correct. Here we use an adjusted computer code, which also puts out all individual Monte Carlo (MC) chains, and derives sedimentation rates and their variability directly from these individual (MC) chains, which yields more precise results than using the distributions of these. The modelling results are presented in Fig. 9. The data set shows a single inversion of the mean ages, but none when uncertainty is considered. Therefore, the age-depth model was created with rather few resampling attempts for stratigraphically consistent data. It can be seen that the applied ADmin age-depth model is sensitive to changes in luminescence age with depth, which resulted in a nonlinear age-depth function, indicating variable sedimentation rates (SRs), at least within the error limits of the technique. The resulting SRs are presented in Table S1 and varied between 0.04 and 0.46 mm a^{-1} with median ($\tilde{x}$) and mean ($\bar{x}$) values of 0.13 and 0.18 mm a^{-1}, respectively.

In order to reliably estimate past atmospheric dust flux (Albani *et al.* 2015), we calculated the mass accumulation rate (MAR) (Kohfeld & Harrison 2003) for the Nosak site. Reconstructing dust MARs from loess deposits is critical to understanding past atmospheric mineral dust activity and requires accurate independent age models from loess deposits. In the territory of Serbia, except for the dust MAR investigations focused on the last glacial–interglacial cycle (e.g. Újvári *et al.* 2010; Stevens *et al.* 2011; Perić *et al.* 2019), thus far, no such studies have been conducted. Hence, we use the SRs provided by the ADmin age-depth modelling to calculate the MAR for the Nosak loess-palaeosol section. Again, it has to be pointed out that the resolution of luminescence ages is not sufficient to allow for robust interpretation at a millennial level.

The aeolian MAR (g m^{-2} a^{-1}) (Kohfeld & Harrison 2003) was calculated using the following equation:

$$\mathrm{MAR} = \mathrm{SR} \times f_{\mathrm{eol}} \times \mathrm{BD} \quad (1)$$

where SR is the sedimentation rate (m a^{-1}), f_{eol} is the proportion of the sediment that is aeolian (assumed value is 1) and BD is bulk density of the loess (g cm^{-3}). The value of dry bulk density (BD) for loess deposits varies in the literature, ranging from 1.3 to 1.7 g cm^{-3} (Újvári *et al.* 2010). For the Chinese Loess Plateau, the measured average BD was 1.48 g cm^{-3} (Kohfeld & Harrison 2003), while for North America the value was 1.45 g cm^{-3} (Muhs *et al.* 2003). Frechen *et al.* (2003) used 1.65 g cm^{-3} for European loess deposits, which appears to be too high when compared to the previously mentioned values. Here we measured the BD directly using the volumetric cylinder method (direct core method). In total, 268 samples were collected by hammering a steel ring (7.0 cm height; 3.8 cm internal diameter; 79.0 cm^{-3} volume) into the face of the undisturbed loess profile. The collected samples were individually packed in plastic zip-lock bags after which they were dried in a microwave oven for 600 s. The dry BD was subsequently calculated using the formula:

$$\rho b = Ms/Vs \quad (2)$$

where ρb is the dry bulk density in mg m^{-3}, Ms is the weight of the dry soil sample in mg, and Vs is the volume of the dry soil sample in m^3 (Han *et al.* 2016).

The measured values range from ~1.22 to 1.83 g cm^{-3} with a mean of 1.491±0.008 g cm^{-3} (Table S1). This equals nearly exactly the most recent measurements of loess dry BD in the Carpathian Basin carried out for the deposits at Dunaföldvár (Hungary) where a mean dry value of 1.497±0.079 g cm^{-3} was determined (Újvári *et al.* 2010). Hence, we use the dry BD of 1.49 g cm^{-3} for the MAR calculations in this study.

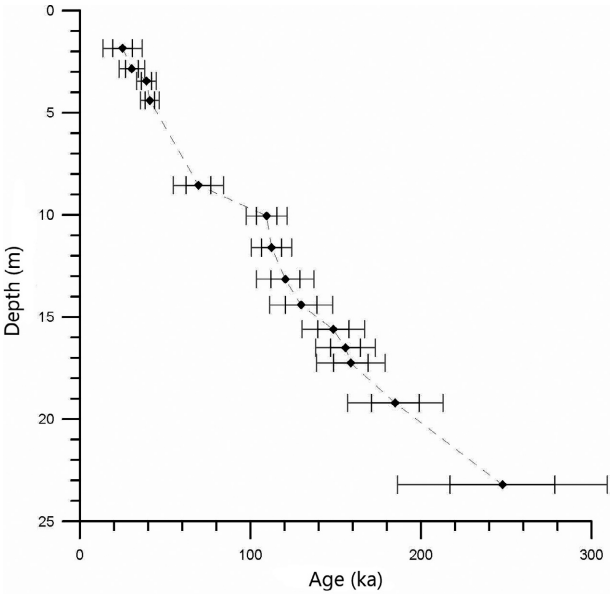

Fig. 9. Age modelling results and $pIRIR_{200, 290}$ ages from Nosak. The results were obtained using the ADmin age-depth modelling method specifically developed for treating luminescence data (Zeeden *et al.* 2018). The original data and uncertainty are plotted as diamonds with error bars: 1-sigma uncertainty as a black line and 2-sigma uncertainty as a grey line. Mean age and uncertainty were linearly interpolated between the age-depth points used in the modelling.

Results

pIRIR chronology

The $pIRIR_{200, 290}$ ages are presented against depth in Fig. 10A as closed and open circles and in Table 2. The calculated ages of the Nosak loess-palaeosol section generally show a consistent increase with depth, ranging from 261±23 ka for sample 133046 (2320 cm depth) to 25±6 ka for the uppermost sample (133059 – 185 cm depth). The proposed multi-millennial chronostratigraphy for Serbian loess (Martinson *et al.* 1987; Lisiecki & Reymo 2005; Thompson & Goldstein 2006; Marković *et al.* 2008, 2015) suggests that the S0 unit corresponds with MIS 1 (0.0–12.1±3.1 ka), L1 most likely covers MIS 2-4 (12.1±3.1 to 80.5±0.9 ka), S1 corresponds to MIS 5 (80.5±0.9 to 129.3±1.0 ka), L2 is equivalent to MIS 6 (129.3±1.0 to 179.2±1.7 ka), S2 is consistent with MIS 7 (179.2±1.7 to 243.0±2.1 ka), L3 is related to MIS 8 (243.0±2.1 to 291.5±0.0 ka), and finally S3 is equivalent to MIS 9 (291.5±0.0 to 337±0.0 ka). In this study, the Last Glacial loess unit L1 is represented by six samples in total, and accumulated between 69±7 and 25±6 ka (MIS 4 – MIS 2). As expected, most of the samples from the upper part of the L1 unit fall into MIS 3, except for the sample 133059, which is at the transition to MIS 2, defined as the Last Glacial Maximum. The uppermost intercalated soil (sample 133058) was dated at 31±4 ka, which suggests that it developed during the late stage of MIS 3. This age shows a good match with the 27±2 ka age of the upper palaeosol of the Last Glacial unit at the Tokaj section in Hungary (Schatz *et al.* 2012), although the soil at Nosak is far less developed, which is possibly the result of diverse palaeoclimatic conditions. Similar ages of the upper palaeosols have been also reported in the Vojvodina region at Surduk: 31.8±3.7 ka (Fuchs *et al.* 2008), Stari Slankamen: 34.4±2.2 ka, (Schmidt *et al.* 2010), Crvenka: 38±4 ka (Stevens *et al.* 2011), and Veliki Surduk at the Titel loess plateau: 34.2±2.4 ka (Perić *et al.* 2019), implying that the soil formation might have had a similar timing across the Carpathian Basin. However, it should be noted that these ages do not necessarily specify the time of soil formation, but rather the time of deposition of the sediment in which the soil subsequently developed (Schatz *et al.* 2012). The two underlying loess layers were dated at 39±3 ka (sample 133057) and 41±3 ka (sample 133056), respectively, falling into MIS 3. Even though this stage is generally characterized by soil formation, loess deposition during MIS 3 has been reported at a number of sites in the Carpathian Basin, most recently at Tokaj in Hungary (e.g. Schatz *et al.* 2012) and Stratzing in Lower Austria (Thiel *et al.* 2011). The $pIRIR_{200, 290}$ age of the lowermost L1 sample is consistent with MIS 4 (69±7 ka).

The S1 soil is represented by two samples and also presents a good pedostratigraphical age control for it was formed during MIS 5 (130–75 ka; Yi *et al.* 2015). The upper sample taken from the upper part of the S1 pedocomplex (sample 133054) was dated at 110±6 ka falling into MIS 5. Sample 133053, recovered from the middle part of S1 (1160 cm depth), is dated at 112±7 ka, (MIS 5e) defined as the peak of the Eemian substage. This is in good agreement with the expected age, confirming the reliability of our results. These results imply that, most likely, the complete last glacial–interglacial cycle is represented at the Nosak site. The penultimate glacial is represented by the L2 unit where five samples were recovered. The uppermost intercalated L2 palaeosol is dated at 130±10 ka indicating that it formed at the transition of MIS 5 and MIS 6. The overlying loess layer displayed an age of 120±10 ka. This date suggests that the L2 loess may have continued deposition well into the MIS 5 stage. The following two samples display a steady age increase with depth; however, the lowermost L2 sample (sample 133048 – 1725 cm depth) displayed an age inversion of ~15 ka.

The S2 palaeosol where one sample was taken at the approximate depth of the palaeontological layer, was dated at 185±13 ka, falling into the transition of MIS 7 to MIS 6. The calculated age also showed a good agreement (within the error limits) with the ESR date (192±5 ka; Fig. 2) of the mandibular tooth of the mammoth skeleton discovered in 2012. The L3 loess, where one sample was recovered from the lower part of the layer, which is affected by hydromorphic features, was dated at 261±23 ka, suggesting that it accumulated during the late phase of MIS 8.

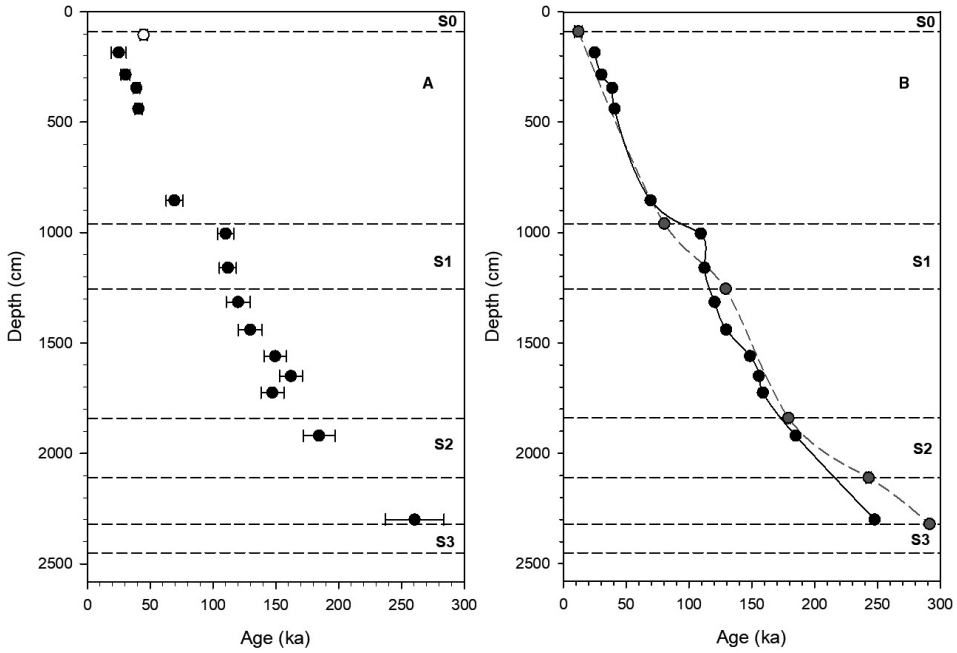

Fig. 10. Age vs. depth for the Nosak site. A. Luminescence ages (the rejected age is presented as an open circle). B. Age models. The black line is based on the $pIRIR_{200, 290}$ ages and the grey dashed line represents the age model based on connecting the stratigraphical boundaries to the marine isotope record (Martinson *et al.* 1987; Thompson & Goldstein 2006). See text for details.

Mass accumulation rates

The calculated MARs based on the modelled $pIRIR_{290}$ ages are presented in Fig. 11 and Table S1. Although in most studies the MAR calculations of aeolian sediments are based on the mean ages, according to Leighton *et al.* (2014), this can result in misinterpretations of the luminescence ages. Accordingly, we include the results for the minimum MAR values. The resulting MARs show the data structure where jumps in ages correspond to low MARs and similar ages relate to higher MARs. Whether this is always a true representation of MARs or partly the result of luminescence age uncertainty is here not perfectly clear (Perić *et al.* 2019). The MAR estimates range between 56 and 684 g m^{-2} a^{-1} ($\tilde{x}$ = 196 g m^{-2} a^{-1} and $\bar{x}$ = 265 g m^{-2} a^{-1}; minimum values $\tilde{x}$ = 85 g m^{-2} a^{-1} and $\bar{x}$ = 105 g m^{-2} a^{-1}). For the penultimate glacial period the MAR record is characterized by high variability with values ranging from 97 to 450 g m^{-2} a^{-1} (minimum values 61 to 95 g m^{-2} a^{-1}), peaking between ~160 and 185 ka, during the MIS 6 stage. During MIS 5, the MARs on average display lower values reaching 293 g m^{-2} a^{-1} (minimum $\bar{x}$ = 127 g m^{-2} a^{-1}); however, a rapid increase was observed between ~112 and 120 ka. For the Last Glacial the absolute values range from 262 to 682 g m^{-2} a^{-1} (minimum values 106 to 204 g m^{-2} a^{-1}) peaking between 39 and 41 ka. The weighted mean for the interval covering ~25 to 31 ka is 262 g m^{-2} a^{-1} (minimum $\bar{x}$ = 106 g m^{-2} a^{-1}). Similar values for the Carpathian Basin were reported by Újvári *et al.* (2010) for the period between 12 and 28 ka where the calculated MARs were $\tilde{x}$ = 338 and 417 g m^{-2} a^{-1} (range 150–1422 g m^{-2} a^{-1}). For the loess sites in Serbia average values of MARs range from 150 to 510 g m^{-2} a^{-1}: Batajnica 329; Irig 192; Mošorin 395; Petrovaradin 174; Stari Slankamen 168; Surduk 434; Susek 150 and Titel 510 g m^{-2} a^{-1} (Újvári *et al.* 2010), which generally agrees with the calculated MARs at Nosak. It has been reported by both Frechen *et al.* (2003) and Újvári *et al.* (2010) that lower MARs occur in plain and hill slope settings while the highest MAR values appear to be related to terrace deposition in major river systems. This also seems to be the case at Nosak. This suggests that, at a broad scale, during the Last Glacial cycle, the past atmospheric dust activity may have had a similar trend across the Carpathian Basin.

Discussion

Lithology and stratigraphical position of the luminescence samples are presented in Fig. 2 and the post-IR IRSL ages are presented in Fig. 10A as a function of depth. The dose rates do not show any detectable trend with depth, which is also noticeable in the D_e values and the resulting ages. Figure 10B shows the expected age model according to the ages of the MIS transitions (Martinson *et al.* 1987; Thompson & Goldstein 2006) together with the calculated age model for the Nosak sequence. It can be seen that the $pIRIR_{200, 290}$ ages

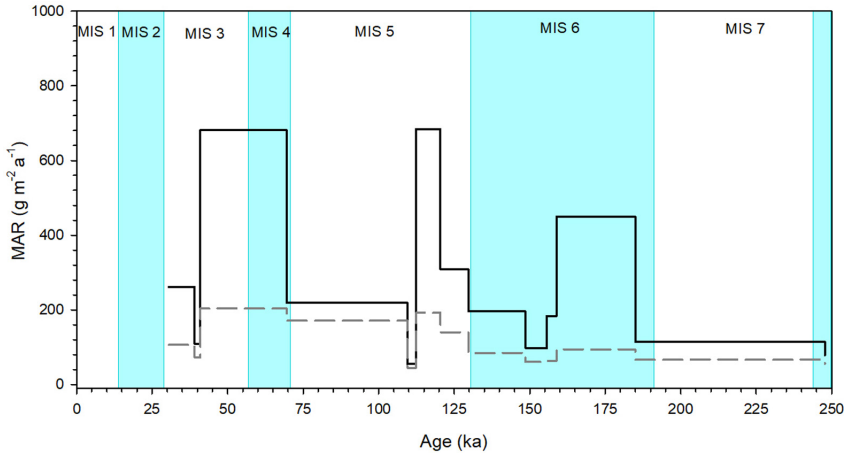

Fig. 11. Dust mass accumulation rate (MAR) as a function of age for the Nosak site. The MAR values were obtained using the model of Zeeden *et al.* (2018). The solid black line represents the mean MAR values, while the dashed grey line shows the lower 95% probability. Because some ages are almost overlapping, the values of the upper 95% probability of the MARs are in some intervals very high, which is why they are not presentable in this figure. These high MARs are not always realistic but represent the result of not assuming strict sedimentation boundaries. For details see text and Table S1. [Colour figure can be viewed at www.boreas.dk]

partially display a good agreement with the expected ages and are stratigraphically consistent, however, with some noticeable irregularities. Most ages of the L1 loess are coherent with MIS 2 and MIS 3, suggesting that the entire Last Glacial–interglacial cycle is represented at the Nosak site. While it can be observed that our luminescence dates show a very good agreement from the top to the base of L1, the upper S1 sample displayed a higher age than expected from the MIS chronostratigraphy (Fig. 10B). In this case, it is conceivable that the proposed multi-millennial chronostratigraphy for Serbian loess does not entirely apply to the Nosak loess-palaeosol sequence. In several studies, it has been discussed that there are reasons why the accuracy of the MIS based correlation ages should be taken with caution. It is known that soil development into underlying glacial-age loess has been detected in many loess regions, which could potentially conceal the true depositional age of sediments at a soil–loess boundary (e.g. Liu *et al.* 2004). Moreover, it is often the case that correlation based models do not consider postdepositional processes such as mixing, erosion or bioturbation (Stevens *et al.* 2006; Buylaert *et al.* 2007; Lai *et al.* 2007; Lai 2010), which can result in very large inconsistencies between correlation and independent age models (Stevens *et al.* 2008, 2011). Here we argue that in the case of the sample 133054 taken at the S1–L1 boundary, the proposed chronostratigraphy might be in error. It is possible that soil development continued to a later stage than is generally accepted from the marine record, which resulted in the difference to the expected age. Nevertheless, despite the offset, the calculated age shows an acceptable agreement with the proposed chronostratigraphy within the uncertainty limits (1-sigma uncertainty is reported here). The ages for the L2 loess layer show a steady increase with depth and are in good accordance with the MIS chronostratigraphy. This stratigraphical interpretation is largely confirmed by the published post-IR ages of Stari Slankamen (from 186±11 to 146±9 ka) presented by Schmidt *et al.* (2010). However, the lowermost L2 sample (133048) displayed an age drop of ~15 ka compared to the overlying sample. Here we have to consider the possibility that there might be a discontinuity above the sample where the age inversion was observed. It is possible that there was a break in sedimentation or an erosion event around 170–165 ka. After such an event, the underlying soil might have been reworked, which would result in the resetting of the luminescence signal. Unfortunately, the sampling resolution is not sufficient to identify the extent and precise position of this hiatus and these require additional investigation. Still, the calculated age displayed a satisfactory agreement with the expected age (within the error limit), which allowed us to include it in the age-depth modelling.

Marković *et al.* (2014a) proposed that the S1 unit represents a single pedocomplex and is equivalent to MIS 5. Nevertheless, contrary to these conclusions, the initial low field magnetic susceptibility record (for details see Marković *et al.* 2014a) and our data suggest that S1 comprises three subunits: (i) S1SS2 (corresponding with the S1 pedocomplex previously described by Marković *et al.* (2014a)), (ii) a thin, weakly developed palaeosol (S1SS1), and (iii) a thin loess layer (S1LL1). The S1SS1 and S1LL2 subunits can be described as a palaeosol–loess 'couple', which was previously interpreted as the oldest part of the composite last glacial loess L1, or the introductory part of MIS 4 (Marković *et al.* 2014a). However, according to the pIRIR age of sample 133054 (110±6 ka), this part of the sequence falls into MIS 5.

This can be explained by the proximity of the main dust source (Danube alluvial plain) and high dust input during the latter stage of MIS 5, contributing to the distinctive composition of the S1 pedocomplex at Nosak.

Based on the presented luminescence age of the overlying loess unit (260±23 ka; Fig. 2), the lowermost palaeosol (S2SS2 according to Marković *et al.* 2014a) previously correlated with the oldest part of MIS 7 needs to be re-interpreted as S3 and equivalent to MIS 9. Given the fact this loess layer is represented by only one age, which is not sufficient to draw a definitive conclusion, we cannot exclude the possibility of age overestimation for sample 133046 due to bioturbation and that the palaeosol we labelled as S3 does not represent MIS 7. It is also conceivable that the soil development started earlier than suggested by the MIS record; however, we find it more probable that the L3 sample slightly underestimates the true age. It is possible that the soil development during MIS 9 resulted in mixing and bioturbation of the overlying loess that caused the resetting of the luminescence signal during this period. This would result in an age underestimation that cannot be detected by the MIS chronostratigraphy. Thus, based on the calculated age and field observations, we conclude that the loess layer previously indicated as S2LL1 should, most likely, be re-labelled as L3 corresponding with MIS 8. This is the main re-interpretation of the stratigraphical model presented by Marković *et al.* (2014a).

The arguments stated above illustrate the complexity of the establishment of accurate chronologies for loess sites when applying age models based on correlation. This is especially true for luminescence based models where the uncertainties about the time of the last signal resetting caused by postdepositional processes may be very significant. While these uncertainties can impact the luminescence age model considerably, a correlation based age model would not be able to detect such variations. Similar problems in this region were reported by Stevens *et al.* (2011) for the Crvenka loess-palaeosol sequence where age underestimation and reversals were observed for several samples. These issues were attributed mainly to postdepositional processes (i.e. mixing, erosion, bioturbation and sedimentation changes). It would seem that this problem is not confined solely to the Nosak site, but may have also played a major role in the development of further loess sites in the Middle Danube Basin. In order to definitively identify such problems, high sampling resolution dating is required. Nevertheless, in the case of the Nosak site, we argue that postdepositional processes are, most likely, the main cause for the observed discrepancies in the age model.

The MAR values at the Nosak site are highly variable over the last three glacial–interglacial cycles, demonstrating the importance of local conditions and the changing position of the Danube River and its alluvial plain as the main silt source (towards the south). Generally, our MARs displayed higher and more variable values during the glacial periods when compared with interglacial intervals, which is consistent with the findings of e.g. Zhang *et al.* (1999, 2002), Kohfeld & Harrison (2003), Sun *et al.* (2005), and Stevens *et al.* (2011). The MARs displayed values of $\tilde{x}$ = 195 and 265 g m^{-2} a^{-1} (minimum values $\tilde{x}$ = 85 and 105 g m^{-2} a^{-1}), which is in good accordance with the results reported by Újvári *et al.* (2010) for the Carpathian Basin. However, these values are considerably lower than reported for other European sites. One of the main reasons for this is that loess accumulations in the Carpathian basin are mostly represented by loess plateaus, contrary to other European regions where loess formation is usually related to slope sedimentation conditions (Marković *et al.* 2018). Frechen *et al.* (2003) reported MARs around the River Rhine ranging from 800 to 3200 g m^{-2} a^{-1}. At Wallertheim (terrace) the reported mean value was 6930 g m^{-2} a^{-1} (Wintle & Brunnacker 1982) while for the Nussloch site the values ranged from 1213 to 6129 g m^{-2} a^{-1} (Lang *et al.* 2003). The lowest MARs were reported in Belgium at Kesselt (Van den Haute *et al.* 1998), Remicourt (Frechen *et al.* 2003) and Rocourt (Wintle 1987) and in eastern France at Achenheim (Rousseau *et al.* 1998) represented by three slope sites and one terrace location where the values range from 93 to 450 g m^{-2} a^{-1}. Extremely high MARs were observed at Grubgraben in Lower Austria (Damblon *et al.* 1996) and Paks in Hungary (Frechen *et al.* 1997) with values between 1600 and 3200 g m^{-2} a^{-1} along the Danube. The comparison between the MARs at Nosak and those at other European loess sites shows, in some cases, significant inconsistencies. The disagreements are partially the result of different dating methods, BDs and SRs used in the MAR calculations, partially because various time periods are investigated but probably mostly due to the different local conditions. In order to make a realistic comparison (and determine the degree to which local conditions impact the MAR values more accurately) it would be necessary to calculate MARs for similar types of loess profiles, applying the same dating method, and averaging over the same time interval. However, this would require an extensive study that would necessitate an enormous amount of resources and time, which is, at least currently, not possible. Nonetheless, the general conclusion that can be drawn from these comparisons is that the amplitudes of MAR records for the majority of the investigated sites in Europe display similar glacial–interglacial fluctuations. Furthermore, it is apparent that, as already stated, lower MARs occur in plain and hill slope settings while the highest MAR values are found at sites along major rivers in Europe (e.g. Rhine and Danube), which is also applicable for the Nosak site.

Based on the calculated pIRIR ages a rapid MAR increase is observed at Nosak during MIS 4 peaking ~70 ka, with values ranging from 219 to 682 g m^{-2} a^{-1} (minimum 171–204 g m^{-2} a^{-1}). However, the MARs

remain high also during MIS 3, although they are much more variable (Fig. 11). In spite of the proximity of the Nosak site and the loess sequences in Vojvodina, it is obvious that the maximumMARs during the Last Glacial period appear to occur during different time intervals. At most investigated sites in the Vojvodina region, maximum MAR values were recorded during MIS 2 while during MIS 3 lower and more constant MARs were detected (e.g. Újvári *et al.* 2010; Perić *et al.* 2019). Unfortunately, we are missing samples for MIS 1 and MIS 2, which is why we cannot have certainty whether the MARs at Nosak truly peak during MIS 3 or if the values may have been higher in MIS 2. Even though the average MARs display lower values during MIS 5, a short term peak was observed between ~112 and 120 ka during MIS 5e. However, between 109 and 112 ka the MARs display a rapid decrease to a value of 56 g m^{-2} a^{-1} (minimum 45 g m^{-2} a^{-1}). Such fluctuations could be the result of changes in the main silt source, wind intensity and direction shifts, activation of an additional silt source or a combination of these factors.

For the high MAR values during the MIS 3 stage at Nosak, we cannot exclude or prove site-specific reasons as similar results have also been reported at other sites in the Carpathian Basin, most notably at Surduk (Fuchs *et al.* 2008), Süttö (Novothny *et al.* 2009, 2011) and Paks (Thiel *et al.* 2014), or for the MAR peak during MIS 5. Higher transport rates, more efficient trapping, palaeowind intensity (e.g. Gavrilov *et al.* 2018) or the relative proximity of the Danube River may have contributed to the apparently continuous loess accumulation at the Nosak site. The high accumulation rates could also be an artefact of dating uncertainty (see Perić *et al.* 2019 for uncertainty) or of sampling resolution,which is here not high enough to detect all the breaks and decreases in dust input over time, but may also represent a true feature.

According to the presented MARs, it is obvious that loess accumulation at Nosak was highly variable. This is contrary to most assumptions where continuous loess deposition is assumed. Furthermore, loess profiles mostly appear to have a uniform composition, which is why hiatuses are often very hard to detect solely by stratigraphical interpretation. This also seems to be the case at Nosak. In order to have a more complete insight into the extent to which hiatuses and postdepositional processes affected the formation of the Nosak profile, further dating is needed, with a higher sampling resolution, especially for the uppermost part of the L1 loess.

The main palaeo-environmental pattern of the Nosak loess sequence is evidence of progressive aridization of the reconstructed ancient landscapes. The lower penultimate interglacial S2 pedocomplex indicates more humid conditions than during the formation of the last interglacial S1 pedocomplex. This may be the consequence of more shallow groundwater at the Nosak loess sequence, which can support the existence of a more intensive vegetation cover during the enhanced pedogenesis of the older pedocomplexes.

Conclusions

Our study presents the first pIRIR chronology over the last three glacial–interglacial cycles for northeastern Serbia. The $pIRIR_{200,\ 290}$ based age model is in good agreement with the geological situation; however, it suggests the need for a partial revision of the chronostratigraphical model proposed by Marković *et al.* (2014a) for the Nosak loess-palaeosol sequence. The presented results suggest a chronological re-interpretation of the oldest palaeosol-loess couple (previously indicated as S2SS2 and S2LL1 by Marković *et al.* 2014a) and their stratigraphical re-labelling as L3 and S3 respectively. Our results also imply that the S1–L1 boundary is located stratigraphically higher in the sequence than proposed in previous studies (Marković *et al.* 2014a; Muttoni *et al.* 2018). Thus, the S1 soil development continued to a later stage than previously assumed and here we suggest a revision of the S1–L1 boundary and a reinterpretation of the S1 pedocomplex composition.

The mean MAR value of 265 g m^{-2} a^{-1} shows a good agreement with the MAR values of other sites in the Carpathian Basin, although our model shows much higher variability especially during the Last Glacial. This discrepancy might be the result of the applied age-depth modelling methodology where each method makes diverse assumptions over loess accumulation rates (or not) and the weight given to individual age points but could also represent a true feature. Contrary to most of the investigated sites in the region (e.g. Újvári *et al.* 2010; Stevens *et al.* 2011), very high MAR values were recorded during the MIS 3 stage, which may be a consequence of missing samples from the upper part of the L1 loess at the Nosak site. However, at this point, we cannot absolutely exclude the possibility that site-specific reasons caused peak MAR values during the MIS 3 stage as similar results have been reported at other loess-palaeosol sequences in the Carpathian Basin.

In order to obtain a better understanding of the deposition evolution of the Nosak sequence and establish a more accurate chronostratigraphy (especially for the transition zone between the L1 loess layer and the pedocomplex S1), further studies are required by applying pIRIR measurements with a higher sampling resolution. Additionally, for the upper part of the L1 loess unit, quartz OSL measurements are needed as these are considered to be more suitable for younger samples. This would allow us to gain more insights into the deposits of the Last Glacial period and atmospheric dust flux estimates at the Nosak site.

Acknowledgements. – The authors would like to thank Dr Miomir Korać and Dr Nemanja Mrdjić from the Viminacium Archeological

Park for their help during fieldwork. We thank Dr Jan-Pieter Buylaert for the delivery of the prepared luminescence samples. We also express our gratitude to the reviewer Dr Frank Lehmkuhl and the anonymous reviewer for their useful comments and suggestions on the original manuscript. We especially thank Prof. Jan A. Piotrowski for his help in the final correction of this paper.

Author contributions. – Sample collection: SBM; gammaspectrometry measurements: CT and ASM; sample preparation: CT and ZMP; luminescence measurements: GS and ZMP; age-depth modelling: CZ; data analysis: ZMP and SBM; data presentation: ZMP and SBM; original draft preparation: ZMP, SBM and MBG; review and editing: all authors. The authors declare no conflict of interest.

References

Albani, S., Mahowald, N. M., Winckler, G., Anderson, R. F., Bradtmiller, L. I., Delmonte, B., François, R., Goman, M., Heavens, N. G., Hesse, P. P., Hovan, S. A., Kang, S. G., Kohfeld, K. E., Lu, H., Maggi, V., Mason, J. A., Mayewski, P. A., McGee, D., Miao, X., Otto-Bliesner, B. L., Perry, A. T., Pourmand, A., Roberts, H. M., Rosenbloom, N., Stevens, T. & Sun, J. 2015: Twelve thousand years of dust: the Holocene global dust cycle constrained by natural archives. *Climate of the Past 11*, 869–903.

Antoine, P., Rousseau, D. D., Fuchs, M., Hatté, C., Gautier, C., Marković, S. B., Jovanović, M., Gaudeenyi, T., Moine, O. & Rossignol, J. 2009: High resolution record of the last climatic cycle in the Southern Carpathian basin (Surduk, Vojvodina, Serbia). *Quaternary International 198*, 19–36.

Blaauw, M. & Christen, J. A. 2011: Flexible palaeoclimate age-depth models using an autoregressive gamma process. *Bayesian Analysis 6*, 457–474.

Bøtter-Jensen, L., Thomsen, K. J. & Jain, M. 2010: Review of optically stimulated luminescence (OSL) instrumental developments for retrospective dosimetry. *Radiation Measurements 45*, 253–257.

Buylaert, J.-P., Jain, M., Murray, A. S., Thomsen, K. J., Thiel, C. & Sohbati, R. 2012: A robust feldspar luminescence dating method for Middle and Late Pleistocene sediments. *Boreas 41*, 435–451.

Buylaert, J.-P., Murray, A. S., Gebhardt, A. C., Sohbati, R., Ohlendorf, C., Thiel, C., Wastegård, S. & Zolitschka, B. 2013: Luminescence dating of the PASADO core 5022-1D from Laguna Potrok Aike (Argentina) using IRSL signals from feldspar. *Quaternary Science Reviews 71*, 70–80.

Buylaert, J.-P., Murray, A. S., Vandenberghe, D., Vriend, M., De Corte, F. & Van den haute, P. 2007: Optical dating of Chinese loess using sand-sized quartz: establishing a time frame for Late Pleistocene climate changes in the western part of the Chinese Loess Plateau. *Quaternary Geochronology 3*, 99–113.

Buylaert, J.-P., Yeo, E.-Y., Thiel, C., Yi, S., Stevens, T., Thompson, W., Frechen, M., Murray, A. & Lu, H. 2015: A detailed post-IR IRSL chronology for the last interglacial soil at the Jingbian loess site (northern China). *Quaternary Geochronology 30*, 194–199.

Damblon, F., Haesaerts, P. & van den Pflicht, J. 1996: New datings and considerations on the chronology of Upper Palaeolithic sites in the Great Eurasiatic Plain. *Préhistoire Européenne 9*, 177–231.

Dimitrijević, V., Mrdjić, N., Korać, M., Chu, S., Kostić, D., Jovičić, M. & Blackwell, B. A. B. 2015: The latest steppe mammoths (Mammuthus trogontherii (Pohlig)) and associated fauna on the Late Middle Pleistocene steppe at Nosak, Kostolac Basin, Northeastern Serbia. *Quaternary International 379*, 14–27.

Frechen, M., Horváth, E. & Gábris, G. 1997: Geochronology of Middle and Upper Pleistocene loess sections in Hungary. *Quaternary Research 48*, 291–312.

Frechen, M., Oches, E. A. & Kohfeld, K. E. 2003: Loess in Europe - mass accumulation rates during the Last Glacial Period. *Quaternary Science Reviews 22*, 1835–1857.

Fuchs, M., Rousseau, D.-D., Antoine, P., Hatté, C., Gauthier, C., Marković, S. & Zoeller, L. 2008: Chronology of the Last Climatic Cycle (Upper Pleistocene) of the Surduk loess sequence, Vojvodina, Serbia. *Boreas 37*, 66–73.

Gavrilov, M. B., Marković, S. B., Schaetzl, R. J., Tošić, I. A., Zeeden, C., Obreht, I., Sipos, G., Ruman, A., Putniković, S., Emunds, K., Perić, Z., Hambach, U. & Lehmkuhl, F. 2018: Prevailing surface winds in Northern Serbia in the recent and past time periods; modern- and past dust deposition. *Aeolian Research 31*, 117–129.

van Gorp, W., Veldkamp, A., Temme, A. J. A. M., Maddy, D., Demir, T., van der Schriek, T., Reimann, T., Wallinga, J., Wijbrans, J. & Schoorl, J. 2013: Fluvial response to Holocene volcanic damming and breaching in the Gediz and Geren rivers, western Turkey. *Geomorphology 201*, 430–448.

Guérin, G., Mercier, N. & Adamiec, C. 2011: Dose-rate conversion factors: update. *Ancient TL 29*, 5–8.

Han, Y. Z., Zhang, J. W., Mattson, K. G., Zhang, W. D. & Weber, T. A. 2016: Sample sizes to control error estimates in determining soil bulk density in California forest soils. *Soil Science Society of America Journal 80*, 756–764.

Huntley, D. J. & Lamothe, M. 2001: Ubiquity of anomalous fading in K-feldspars and the measurement and correction for it in optical dating. *Canadian Journal of Earth Sciences 38*, 1093–1106.

Kang, S., Roberts, H. M., Wang, X., An, Z. & Wang, M. 2015: Mass accumulation rate changes in Chinese loess during MIS 2, and asynchrony with records from Greenland ice cores and North Pacific Ocean sediments during the Last Glacial maximum. *Aeolian Research 19B*, 251–258.

Kars, R. H., Reimann, T., Ankjærgaard, C. & Wallinga, J. 2014: Bleaching of the post-IR IRSL signal: new insights for feldspar luminescence dating. *Boreas 43*, 780–791.

Kohfeld, K. E. & Harrison, S. P. 2003: Glacial-interglacial changes in dust deposition on the Chinese Loess Plateau. *Quaternary Science Reviews 22*, 1859–1878.

Kukla, G. 1987: Loess stratigraphy in Central China. *Quaternary Science Reviews 6*, 191–219.

Kukla, G. & An, Z. 1989: Loess stratigraphy in Central China. *Palaeogeography, Palaeoclimatology, Palaeoecology 72*, 203–225.

Lai, Z. P. 2010: Chronology and upper dating limit for loess samples from Luochuan section in the Chinese Loess Plateau using quartz OSL SAR. *Journal of Asian Earth Sciences 37*, 176–185.

Lai, Z. P., Wintle, A. G. & Thomas, D. S. G. 2007: Rates of dust deposition between 50 ka and 20 ka revealed by OSL dating at Yuanbao on the Chinese Loess Plateau. *Palaeogeography, Palaeoclimatology, Palaeoecology 248*, 431–439.

Lang, A., Hatté, C., Rousseau, D. D., Antoine, P., Fontugne, M., Zöller, L. & Hambach, U. 2003: High-resolution chronologies for loess: comparing AMS ^{14}C and optical dating results. *Quaternary Science Reviews 22*, 953–959.

Lauer, T., Frechen, M., Vlaminck, S., Kehl, M., Lehndorff, E., Shahriari, A. & Khormali, F. 2017: Luminescence-chronology of the loess palaeosol sequence Toshan, Northern Iran - A highly resolved climate archive for the last glacial-interglacial cycle. *Quaternary International 429 B*, 3–12.

Leighton, C. L., Thomas, D. S. G. & Bailey, R. M. 2014: Reproducibility and utility of dune luminescence chronologies. *Earth-Science Reviews 129*, 24–39.

Li, B. & Li, S.-H. 2011: Luminescence dating of K-feldspar from sediments: A 548 protocol without anomalous fading correction. *Quaternary Geochronology 6*, 468–479.

Lisiecki, L. E. & Raymo, M. E. 2005: A Pliocene-Pleistocene stack of 57 globally distributed benthic d 18O records. *Paleoceanography 20*, PA1003, https://doi.org/10.1029/2004pa001071

Lister, A. M., Dimitrijević, V., Marković, Z., Knežević, S. & Mol, D. 2012: A skeleton of 'steppe' mammoth (*Mammuthus trogontherii* (Pohlig)) from Drmno, near Kostolac, Serbia. *Quaternary International 276/277*, 129–144.

Liu, Q. S., Banerjee, S. K., Jackson, M. J., Chen, F. H., Pang, Y. X. & Zhu, R. X. 2004: Determining the climatic boundary between the Chinese loess and palaeosol: evidence from aeolian coarse-grained magnetite. *Geophysical Journal International 156*, 267–274.

Marković, S. B., Bokhorst, M. P., Vandenberghe, J., McCoy, W. D., Oches, E. A., Hambach, U., Gaudenyi, T., Jovanović, M., Stevens, T., Zöller, L. & Machalett, B. 2008: Late Pleistocene loess-palaeosol sequences in the Vojvodina region, North Serbia. *Journal of Quaternary Science 23*, 73–84.

Marković, S. B., Korać, M., Mrđić, N., Buylaert, J.-P., Thiel, C., McLaren, S. J., Stevens, T., Tomić, N., Petić, N., Jovanović, M., Vasiljević, D. A., Sümegi, P., Gavrilov, M. B. & Obreht, I. 2014a: Palaeoenvironment and geoconservation of mammoths from the Nosak loess-palaeosol sequence (Drmno, Northeastern Serbia): Initial results and perspectives. *Quaternary International 334–335*, 30–39.

Marković, S., Hambach, U., Stevens, T., Jovanović, M., O'Hara-Dhand, K., Basarin, B., Lu, H., Smalley, I., Buggle, B., Zech, M., Svirčev, Z., Sümegi, P., Milojković, N. & Zöller, L. 2012: Loess in the Vojvodina region (northern Serbia): an essential link between European and Asian Pleistocene environments. *Netherlands Journal of Geosciences 91*, 173–188.

Marković, S. B., Oches, E. A., McCoy, W. D., Frechen, M. & Gaudenyi, T. 2007: Malacological and sedimentological evidence for "warm" glacial climate from the Irig loess sequence, Vojvodina. *Serbia. Geochemistry Geophysics Geosystems 8*, Q09008, https://doi.org/10.1029/2006GC001565.

Marković, S. B., Stevens, T., Kukla, G. J., Hambach, U., Fitzsimmons, K. E., Gibbard, P., Buggle, B., Zech, M., Guo, Z., Qingzhen, H., Haibin, W., Dhand, O. K., Smalley, I. J., Újvári, G., Sümegi, P., Timar-Gabor, A., Veres, D., Sirocko, F., Vasiljević, D. A., Jary, Z., Svensson, A., Jović, V., Lehmkuhl, F., Kovàcs, J. & Svirčev, Z. 2015: Danube loess stratigraphy - towards a pan-European loess stratigraphic model. *Earth-Science Reviews 148*, 228–258.

Marković, S. B., Stevens, T., Mason, J., Vandenberghe, J., Yang, S., Veres, D., Újvári, G., Timar-Gabor, A., Zeeden, C., Guo, Z., Hao, Q., Obreht, I., Hambach, U., Wu, H., Gavrilov, M. B., Rolf, C., Tomić, N. & Lehmkuhl, F. 2018: Loess correlations – Between myth and reality. *Palaeogeography, Palaeoclimatology, Palaeoecology 509*, 4–23.

Marković, S. B., Timar-Gabor, A., Stevens, T., Hambach, U., Popov, D., Tomić, N., Obreht, I., Jovanović, M., Lehmkuhl, F., Kels, H., Marković, R. & Gavrilov, M. B. 2014b: Environmental dynamics and luminescence chronology from the Orlovat loess–palaeosol sequence (Vojvodina, northern Serbia). *Journal of Quaternary Science 29*, 189–199.

Martinson, D. G., Pisias, N. G., Hays, J. D., Imbrie, J. L., Moore, T. C. Jr & Shackleton, N. J. 1987: Age dating and the orbital theory of the ice ages: development of a high resolution 0 to 300,000-year chronostratigraphy. *Quaternary Research 27*, 1–29.

Muhs, D. R., Ager, T. A., Bettis, E. A. III, McGeehin, J., Been, J. M., Begét, J. E., Pavich, M. J., Stafford, T. W. Jr & Stevens, D. A. S. P. 2003: Stratigraphy and palaeoclimatic significance of Late Quaternary loessepalaeosol sequences of the Last InterglacialeGlacial cycle in central Alaska. *Quaternary Science Reviews 22*, 1947–1986.

Murray, A. S., Marten, R., Johnston, A. & Martin, P. 1987: Analysis for naturally occurring radionuclides at environmental concentrations by gamma spectrometry. *Journal of Radioanalytical and Nuclear Chemistry 115*, 263–288.

Murray, A. S., Thomsen, K. J., Masuda, N., Buylaert, J.-P. & Jain, M. 2012: Identifying well-bleached quartz using the different bleaching rates of quartz and feldspar luminescence signals. *Radiation Measurements 47*, 688–695.

Muttoni, G., Scardia, G. & Kent, V. D. 2018: Early hominins in Europe: the Galerian migration hypothesis. *Quaternary Science Reviews 180*, 1–29.

Novothny, Á., Frechen, M., Horváth, E., Bradák, B., Oches, E. A., McCoy, W. & Stevens, T. 2009: Luminescence and amino acid racemization chronology and magnetic susceptibility record of the loess-paleosol sequence at Süttö, Hungary. *Quaternary International 198*, 62–76.

Novothny, Á., Frechen, M., Horváth, E., Wacha, L. & Rolf, C. 2011: Investigating the penultimate and last glacial cycles of the Sütto loess section (Hungary) using luminescence dating, high-resolution grain size, and magnetic susceptibility data. *Quaternary International 234*, 75–85.

Obreht, I., Buggle, B., Norm, C., Marković, S. B., Boesel, S., Vandenberghe, D. A. G., Hambach, U., Svirčev, Z., Lehmkuhl, F., Basarin, B., Gavrilov, M. B. & Jović, G. 2014: The Late Pleistocene Belotinac section (southern Serbia) at the southern limit of the European loess belt: Environmental and climate reconstruction using grain size and stable C and N isotopes. *Quaternary International 334/335*, 10–19.

Obreht, I., Zeeden, C., Hambach, U., Veres, D., Marković, S. B., Bösken, J., Svirčev, Z., Bačević, N., Gavrilov, M. B. & Lehmkuhl, F. 2016: Tracing the influence of Mediterranean climate on Southeast Europe during the past 350,000 years. *Scientific Reports 6*, 36334, https://doi.org/10.1038/srep36334.

Obreht, I., Zeeden, C., Hambach, U., Veres, D., Marković, S. B. & Lehmkuhl, F. 2019: A critical reevaluation of palaeoclimate proxy records from loess in the Carpathian Basin. *Earth Science Reviews 190*, 498–520.

Perić, Z., Lagerbäck Adophi, E., Buylaert, J.-P., Stevens, T., Újvári, G., Marković, S. B., Hambach, U., Fischer, P., Zeeden, C., Schmidt, C., Schulte, P., Huayu, L., Shuangwen, Y., Lehmkuhl, F., Obreht, I., Veres, D., Thiel, C., Frechen, M., Jain, M., Vött, A. & Zöller, L. 2019: Quartz OSL dating of late Quaternary Chinese and Serbian loess: a cross Eurasian comparison of dating results and mass accumulation rates. *Quaternary International 502*, 30–44.

Prescott, J. R. & Hutton, J. T. 1994: Cosmic ray contributions to dose rates for luminescence and ESR dating: Large depths and long-term time variations. *Radiation Measurements 23*, 497–500.

Rees-Jones, J. 1995: Optical dating of young sediments using fine-grain quartz. *Ancient TL 13*, 9–13.

Reimann, T., Thomsen, K. J., Jain, M., Murray, A. S. & Frechen, M. 2012: Single-grain dating of young sediments using the pIRIR signal from feldspar. *Quaternary Geochronology 11*, 28–41.

Roberts, H. M. 2012: Testing Post-IR IRSL protocols for minimising fading in feldspars, using Alaskan loess with independent chronological control. *Radiation Measurements 47*, 716–724.

Rousseau, D. D., Zöller, L. & Valet, J. P. 1998: Late Pleistocene climatic variations at Achenheim, France, based on a magnetic susceptibility and TL chronology of loess. *Quaternary Research 49*, 255–263.

Schatz, A.-K., Buylaert, J.-P., Murray, A., Stevens, T. & Scholten, T. 2012: Establishing a luminescence chronology for a palaeosol-loess profile at Tokaj (Hungary): A comparison of quartz OSL and polymineral IRSL signals. *Quaternary Geochronology 10*, 68–74.

Schmidt, E. D., Machalett, B., Marković, S. B., Tsukamoto, S. & Frechen, M. 2010: Luminescence chronology of the upper part of the Stari Slankamen loess sequence (Vojvodina, Serbia). *Quaternary Geochronology 5*, 137–142.

Stevens, T., Armitage, S. J., Lu, H. & Thomas, D. S. G. 2006: Sedimentation and diagenesis of Chinese loess: implications for the preservation of continuous, high resolution climate records. *Geology 34*, 849–852.

Stevens, T., Buylaert, J.-P., Lu, H., Thiel, C., Murray, A., Frechen, M., Yi, S. & Zeng, L. 2016: Mass accumulation rate and monsoon records from Xifeng, Chinese Loess Plateau, based on a luminescence age model. *Journal of Quaternary Science 31*, 391–405.

Stevens, T., Lu, H., Thomas, D. S. G. & Armitage, S. J. 2008: Optical dating of abrupt shifts in the Late Pleistocene East Asian monsoon. *Geology 36*, 415–418.

Stevens, T., Marković, S. B., Zech, M., Hambach, U. & Sümegi, P. 2011: Dust deposition and climate in the Carpathian Basin over an independently dated last glacial-interglacial cycle. *Quaternary Science Reviews 30*, 662–681.

Sun, Y. B., Clemens, S. C., An, Z. S. & Yu, Z. W. 2005: Astronomical timescale and palaeoclimatic implication of stacked 3.6-Myr monsoon records from the Chinese Loess Plateau. *Quaternary Science Reviews 25*, 33–48.

Thiel, C., Buylaert, J.-P., Murray, A., Terhorst, B., Hofer, I., Tsukamoto, S. & Frechen, M. 2011: Luminescence dating of the Stratzing loess profile (Austria) - testing the potential of an elevated temperature post-IR IRSL protocol. *Quaternary International 234*, 23–31.

Thiel, C., Horváth, E. & Frechen, M. 2014: Revisiting the loess/palaeosol sequence in Paks, Hungary: a post-IR IRSL based chronology for the 'Young Loess Series'. *Quaternary International 319*, 88–98.

Thompson, L. G. & Goldstein, S. L. 2006: A radiometric calibration of the SPECMAP timescale. *Quaternary Science Reviews 25*, 3207–3215.

Thomsen, K. J., Murray, A. S., Jain, M. & Bøtter-Jensen, L. 2008: Laboratory fading rates of various luminescence signals from feldspar-rich sediment extracts. *Radiation Measurements 43*, 1474–1486.

Tomić, N., Marković, S. B., Korać, M., Mrđić, N., Hose, T. A., Vasiljević, D. A., Jovičić, M. & Gavrilov, M. B. 2015: Exposing mammoths - from loess research discovery to public palaeontological park. *Quaternary International 372*, 142–150.

Újvári, G., Kovács, J., Varga, G., Raucsik, B. & Marković, S. B. 2010: Dust flux estimates for the Last Glacial Period in East Central Europe based on terrestrial records of loess deposits: a review. *Quaternary Science Reviews 29*, 3157–3166.

Újvári, G., Molnar, M., Novothny, A., Pall-Gergely, B., Kovács, J. & Varhegyi, A. 2014: AMS ^{14}C and OSL/IRSL dating of the Dunaszekcso loess sequence (Hungary): chronology for 20 to 150 ka and implications for establishing reliable age-depth models for the last 40 ka. *Quaternary Science Reviews 106*, 140–154.

Van den Haute, P., Vancraeynest, L. & de Corte, F. 1998: The late Pleistocene loess deposits and palaeosols of eastern Belgium: new TL age determinations. *Journal of Quaternary Science 13*, 487–497.

Wintle, A. G. & Brunnacker, K. 1982: Ages of volcanic tuff in Rheinhessen obtained by thermoluminescence dating of loess. *Naturwissenschaften 69*, 181–183.

Wintle, A. G. 1987: Thermoluminescence dating of loess. *Catena Supplement 9*, 103–114.

Wintle, A. G. & Murray, A. S. 2006: A review of quartz optically stimulated luminescence characteristics and their relevance in single-aliquot regeneration dating protocols. *Radiation Measurements 41*, 369–391.

Yi, S., Buylaert, J.-P., Murray, A. S., Lu, H., Thiel, C. & Zeng, L. 2016: A detailed post-IR IRSL dating study of the Niuyangzigou loess site in northeastern China. *Boreas 45*, 644–657.

Yi, S., Buylaert, J.-P., Murray, A. S., Thiel, C., Zeng, L. & Lu, H. 2015: High resolution OSL and post-IR IRSL dating of the last interglacial-glacial cycle at the Sanbahuo loess site (northeastern China). *Quaternary Geochronology 30*, 200–206.

Zeeden, C., Dietze, M. & Kreutzer, S. 2018: Discriminating luminescence age uncertainty composition for a robust Bayesian modelling. *Quaternary Geochronology 43*, 30–39.

Zhang, X. Y., Arimoto, R. & An, Z. S. 1999: Glacial and interglacial patterns for Asian dust transport. *Quaternary Science Reviews 18*, 811–819.

Zhang, X. Y., Lu, H. Y., Arimoto, R. & Gong, S. L. 2002: Atmospheric dust loadings and their relationship to rapid oscillations of the Asian winter monsoon climate: two 250-kyr loess records. *Earth and Planetary Science Letters 202*, 637–643.

Zhao, H. & Li, S.-H. 2005: Internal dose rate to K-feldspar grains from radioactive elements other than potassium. *Radiation Measurements 40*, 84–93.

Supporting Information

Additional Supporting Information may be found in the online version of this article at http://www.boreas.dk.

Table S1. Summary of bulk density measurements and age-depth modelling results.